ACS APPLIED ELECTRONIC MATERIALS

pubs.acs.org/acsaelm Article

Nanomechanical Characterization of Organic Surface Passivation Films on 50 nm Patterns during Area-Selective Deposition

Mattia Pasquali, Stefanie Sergeant, Thierry Conard, Valentina Spampinato, Alessandro Viva, Stefan De Gendt, and Silvia Armini*

Cite This: ACS Appl. Electron. Mater. 2021, 3, 2622−2630 Read Online

ACCESS | Metrics & More | Article Recommendations | Supporting Information

ABSTRACT: Area-selective deposition (ASD) is a "bottom-up" substrate-selective material deposition process, considered as a promising alternative to current "top-down" pattering techniques. The most studied and successful ASD strategies envisage a combination of atomic layer deposition (ALD) and a passivation layer, which prevents material deposition on the non-growth areas. As ASD targets increasingly smaller dimensions, metrology challenges are prominent along with preserving confined film growth. For patterned substrates with nanometric critical dimensions, only a few characterization techniques can be employed to assess the ASD performance. However, these techniques provide no or little insight into the passivation layer. This is a crucial limitation as the blocking film plays a key role in the ASD process. In this work, pulsed force mode atomic force microscopy (AFM) is used to characterize and monitor the quality of the passivation films by measuring the surface energy fluctuations occurring on the patterned substrate undergoing ASD. As the evolution of the relative adhesion force distribution of the sample under ALD conditions is recorded, the octadecanethiol (ODT) coverage on non-growth areas is accurately estimated. The heavily temperature-dependent self-assembled monolayer degradation revealed by the nanomechanical characterization is supported by X-ray photoelectron spectroscopy. As Hf_3N_4 ALD is performed, the top-down scanning electron microscopy investigation is employed to show the strong relationship between ASD quality upon ALD and pulsed force AFM-derived ODT coverage.

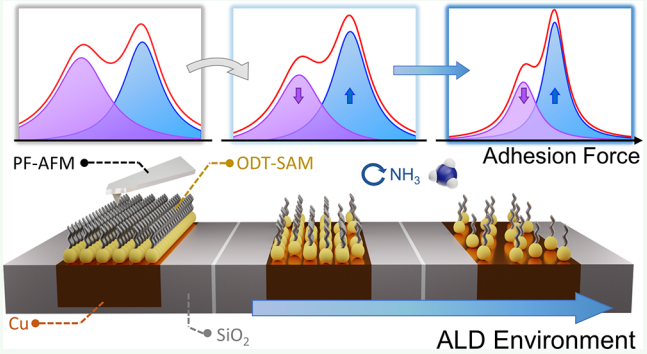

KEYWORDS: *area-selective deposition, self-assembled monolayer, atomic force microscopy, pulsed force mode, tip−sample adhesion force, ASD metrology*

INTRODUCTION

To keep up with Moore's law,[1] device fabrication is facing numerous challenges as a result of the never-ending nanoelectronics downscaling. As the semiconductor industry is approaching the 5 nm node technology, conventional patterning schemes, based on multiple "top-down" lithography and etch steps, cannot meet the ever-increasing requirements for alignment imposed by device miniaturization.[2−4] Area-selective deposition (ASD) can potentially alleviate such manufacturing challenges by enabling bottom-up material deposition. This appealing perspective explains why ASD has gained significant interest from the scientific and technological communities in the last decade.[2,5,6] ASD refers to a substrate-selective process whereby a target film is deposited exclusively on the growth areas with respect to the non-growth areas. This confined deposition is typically achieved by combining surface-sensitive deposition techniques, such as atomic layer deposition (ALD), and an appropriate substrate that offers well-distinguished local surface chemistries.[6−10] Under suitable conditions, ALD starts immediately on the growth area, whereas a nucleation inhibition is observed on the non-growth area, resulting in a successful ASD process. Nevertheless, ALD intrinsic selectivity is usually limited to very few ALD cycles, thus encouraging the ASD community to investigate and study different approaches to widen the deposition process selectivity window. Such methods consist of either activating or passivating the intended areas toward ALD nucleation;[11−20] these are typically referred to as area-activation and area-deactivation strategies, respectively. The latter has been the most widely studied.[6,7]

The area-deactivation scheme envisages ALD blocking functionalities that are selectively grafted[13−18,20−23] or created by a gas/plasma or a wet surface treatment.[11,19,24,25] Regardless

Received: March 8, 2021
Accepted: May 31, 2021
Published: June 10, 2021

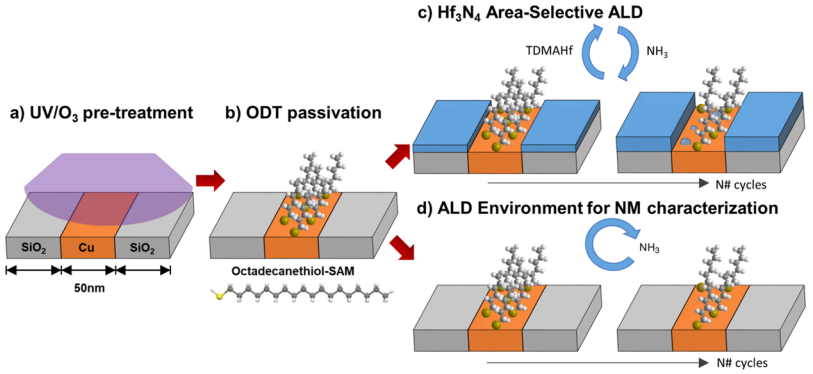

Figure 1. Schematic illustration of the SAM-enabled ASD process. Step 1: (a) 50 nm-wide Cu/SiO_2 lines are exposed to UV/ozone for 10 min. Step 2: (b) selective chemisorption of the ODT-derived SAM is exploited to passivate the metal lines. Step 3: either (c) the Hf_3N_4 ALD is performed or (d) the substrate is exposed to NH_3 half-cycles. In the latter case, Hf_3N_4 deposition is prevented by not dosing the Hf precursor, which facilitates the nanomechanical (NM) characterization by pulsed force atomic force microscopy (AFM).

of how a passivation means is obtained, it prevents ALD nucleation in two ways. First, the blocking layer passivates ALD-reactive surface sites on the growth areas, hence removing favorable spots for material nucleation and deposition. Second, the newly passivated surface generally has a lower surface energy, which hinders the physisorption of ALD precursor molecules, thus extending the nucleation delay. Essentially, a fine tuning of the substrate's surface properties with the creation of a well-defined local chemistry enables the extension of a given ALD process selectivity.[26,27] Nonetheless, as the material deposition continues, undesired particles eventually start to nucleate on the passivated areas. Such selectivity loss is caused by the progressive degradation of the low surface energy passivation moieties, whose underlying mechanisms depend on the nature of the blocking film itself. As an example, if the ASD mask consists of chemisorbed species on the non-growth areas, their progressive desorption during ALD reveals more of the high surface energy substrate, thus allowing nucleation of unwanted particles (Figure 1c).Therefore, the surface properties of the non-growth area are expected to change as more and more molecules are depleted.

We propose an innovative approach to characterize the passivation films by monitoring the surface energy fluctuations occurring on the patterned substrate undergoing ASD. The goal of this work is to shed light on the underlying mechanisms that eventually lead to selectivity loss during an ASD process by providing the scientific and technological communities with a new characterization methodology to monitor the ASD mask during the material deposition process directly on patterned samples. It is well-known that, along with the difficulties in preserving a confined film growth during the ALD process, metrology challenges have risen as ASD is sought at smaller and smaller critical dimensions. Indeed, few characterization techniques are available to assess the selectivity of a given process as a substrate's features approach nanometric dimensions. At such a scale, ASD results are predominantly evaluated and studied by a combination of scanning electron microscopy (SEM), transmission electron microscopy (TEM), energy-dispersive X-ray spectroscopy (EDX), and AFM.[11,13,16,17,19,21,24,25,28−32] In particular, SEM offers a relatively large field image of the patterned substrates, whereas TEM provides images of the ASD film with a resolution of a few nanometers. In addition, EDX measurements taken in conjunction with SEM or TEM enable chemical identification of the investigated samples. As all these measurements are combined together, a clear assessment of the ASD experiment results is possible at critical dimensions as low as 15 nm.[17]

Since self-assembled monolayers (SAMs) are the most extensively employed passivation method for ASD purposes, especially at relevant nanoscale dimensions,[16,17,21,28,29] the proposed characterization method is tested on a SAM-enabled ASD process (Figure 1). In SAM-based ASD processes, the monolayer is selectively grafted to the areas that must be deactivated prior to the ALD. SAM precursors typically consist of a reactive head group that enables the selective chemisorption of the molecules onto the intended surface, a relatively long alkyl chain that provides the driving force to the self-assembly process, and an end group that defines the organic film's surface properties.[33,34] For ASD purposes, hydrophobic CH_3- and CF_3-terminated SAM are preferred since ALD precursor physisorption is hindered on such functional groups. For example, thiol-derived CH_3-terminated SAMs have been largely studied to achieve ASD on SiO_2 versus Cu for nanoelectronics applications.[14,15,22,28,29,34−37]

However, the previously mentioned characterization techniques, namely, TEM, SEM, EDX, and AFM, provide no or little insight into the SAM passivation since these are typically done after ALD despite the blocking film playing a key role in the ASD process. On one hand, since SAM molecules typically consist of an alkyl chain, these cannot be probed by SEM. On the other hand, the monolayer nature of the organic film as well as the damage induced during TEM-sample preparation procedures (e.g., capping layer deposition, focused ion-beam cut), make it extremely difficult to clearly observe a SAM by either TEM or EDX at relevant critical dimensions. In this way, only ∼10 nm-thick multilayer organic films have been visualized.[29] One of the few exceptions to this list is AFM. In literature, studies have reported utilizing AFM to inspect SAM-passivated patterned samples.[38] However, from these measurements, no chemical information can be extracted and it is not possible to understand how the SAM evolves during an ASD process. Consequently, the organic film is typically studied on non-patterned surfaces, whereas only the ASD film is characterized on the patterned substrate. Obviously, being able to monitor and observe the evolution of the SAM during ALD directly on patterned substrates can provide fundamental insights and understanding over SAM-enabled ASD mechanisms.

https://doi.org/10.1021/acsaelm.1c00219
ACS Appl. Electron. Mater. 2021, 3, 2622−2630

We exploit the well-known selective chemisorption of 1-octadecanethiol (ODT) on Cu over SiO_2, in combination with Hf_3N_4 ALD (Figure 1) to address this lack in ASD metrology by proposing an innovative method to characterize the SAM passivation using the example of 50 nm-wide Cu/SiO_2 lines. This goal is achieved by measuring the adhesion force on ODT-coated patterned samples using AFM in the pulsed force mode.[39,40] Pulsed force AFM allows one to record the force−distance curve as the microscope tip is approaching and is withdrawn from the sample surface. In this way, it is possible to simultaneously collect topographical and NM two-dimensional (2D) maps of the analyzed surface[41] at the nanometer scale.[42,43] For these reasons, pulsed force AFM has found many applications in both materials science,[42,44−46] allowing to distinguish between different materials on a given surface (e.g., material recognition in polymer blends), and in biology,[47,48] where single protein loop pairs were successfully resolved.[49]

Hence, the core idea of this study is to visualize and characterize the SAM passivation by exploiting the adhesion force contrast that is expected to rise between the hydrophobic passivated 50 nm-wide Cu lines (low adhesion force) and the hydrophilic SiO_2 lines (high adhesion force). The passivated substrates are also analyzed by pulsed force AFM after being exposed to ALD conditions. In contrast to the Hf_3N_4 ALD process (Figure 1c), no Hf precursor is dosed in this kind of experiment to suppress any material deposition (Figure 1d). This precaution is taken to ease the NM characterization by preventing the creation of a topographical step-profile as well as the introduction of an additional material. Upon thermal treatments and exposure to NH_3 co-reactant equivalent to a given Hf_3N_4 ALD process (Figure 1d), the ODT-coated Cu lines are expected to become less and less hydrophobic because of the organic film progressive degradation. By closely monitoring this adhesion force contrast reduction between passivated-Cu and SiO_2 lines, we aim at getting critical understanding about the SAM evolution during the ASD process. Finally, the ODT-passivated substrates are tested against Hf_3N_4 ALD, unveiling a direct relation between the ASD performance and the pulsed force AFM-derived insights about the organic passivation.

Based on these premises, the proposed NM characterization could be extended to a broad range of ASD systems. The main requirement to be met is the creation of a surface energy gradient as the passivation layer is formed or deposited, which is a condition typically met in area-deactivation ASD schemes. If the surface energy gradient corresponds to a detectable adhesion force contrast between pristine and functionalized areas, the passivation can be monitored by pulsed force AFM measurements, regardless of the blocking layer nature.

EXPERIMENTAL PROCEDURE

Materials. 300 mm Si wafers are provided by SunEdison Semiconductor, whereas ODT and tetrakis(dimethylamido)hafnium (TDMAHf) are supplied by Sigma-Aldrich and used as received. The patterned substrate consists of 50 nm half-pitch (HP) Cu/SiO_2 lines. The liner employed for Cu lines consists of 3 nm TaN deposited by physical vapor deposition (PVD) and 1 nm Ru deposited by chemical vapor deposition. A 6 nm PVD Cu seed layer was used to enable Cu line filling by electrodeposition in an alkaline Cu plating bath followed by reflow and a final 30 s of annealing at 180 °C in He/H_2. A final chemical mechanical planarization (CMP) step was used to remove the Cu overburden, liner, and barrier and to planarize the stack down to the Cu/SiO_2 lines. Immediately after the CMP step, substrates were exposed to UV/ozone for 10 min and transferred to an inert nitrogen atmosphere, where the SAM deposition takes place. The inert atmosphere prevented both Cu oxidation and ODT solution degradation. The SAM film was deposited by submerging the substrates into a 50 mM ODT solution in ethanol. After approximately 48 h, samples were taken out of the ODT solution, rinsed in ethanol, and dried under a nitrogen flow. Finally, the passivated substrates were sealed and immediately transferred to the ALD reactor; this way, sample's exposure to atmosphere was minimized.

Hf_3N_4 ALD was carried out at 100, 120, and 135 °C in a Veeco Savannah 300S reactor placed under a nitrogen atmosphere. Sequential pulses of TDMAHf for 0.300 s and NH_3 for 0.025 s with a 10 s intra-pulse purge step were used to deposit Hf_3N_4. An initial 180 s temperature stabilization step was performed in each process. The TDMAHf precursor was heated up to 75 °C, whereas NH_3 was delivered at room temperature. The average precursor pressures in the reactor were 0.50 ± 0.01 and 2.43 ± 0.25 Torr during TDMAHf and NH_3 dosing, respectively. As mentioned in the introduction, to prevent Hf_3N_4 deposition on samples intended to undergo NM characterization, the TDMAHf dosing step was skipped (Figure 1d). It is worth noticing that skipping the Hf precursor delivery has a negligible impact on the duration of a single ALD cycle. In these processes, the average reactor pressure during NH_3 dosing was 2.11 ± 0.38 Torr. In all processes, a nitrogen carrier flow of 20 sccm was employed to deliver the precursors into the reactor.

Surface Characterization. A commercial Bruker Dimension Icon AFM system was used in the pulsed force mode to obtain 2D topological and NM property maps of the 50 nm-wide Cu/SiO_2 lines by performing peak force quantitative NM analysis.[50] The AFM system was equipped with a HQ-NSC19/AlBs cantilever from MikroMasch, with an uncoated Si tip, the nominal radius of which is 8 nm. The cantilever has 0.5 N/m nominal spring constant and was operated at 2 kHz. The piezo scanner was controlled by a Bruker Nanoscope V feedback controller. To prevent substrate aging, the samples were sealed under N_2 prior to the NM characterization, which was carried out *ex situ* in ambient atmosphere at room temperature. All adhesion force maps were collected at the same resolution (512 × 512 measurement points) across a 1 × 1 μm scanned area, with a pulsed force setpoint (PFS) ranging between 1.5 and 0.1 nN (Supporting Information S1). The adhesion force was defined as the absolute value of the minimum force experienced by the AFM tip during an approach−withdrawn cycle.[42] No correlation was found between topological profiles (Supporting Information S2) and the adhesion properties of the studied samples upon ODT coating, before and after exposure to the NH_3 co-reactant. A first-order polynomial flattening was applied to all AFM images with Nanoscope Analysis v 1.5 software. This was used to convert the maps in ASCII as well, allowing to plot the relative adhesion force distributions (RAFDs) normalized by the applied PFS. Finally, RAFD fitting and peak deconvolution were done with a Matlab signal processing tool made freely available by Tom O'Haver.[51] All RAFDs were fitted by either a two Lorentzian functions or a single Gaussian, depending on whether the distributions are unimodal or bimodal. An RAFD is considered unimodal as the following two criteria are met. First, a single Gaussian function provides a better fitting compared to two Lorentzian functions (i.e., the first fitting has a higher R^2). Second, the distribution is strongly symmetrical. The results of this data analysis are reported in Supporting Information S3.

Self-focusing secondary ion mass spectrometry (SF-SIMS) was used on the patterned substrate for molecular identification purposes. Samples were sealed under N_2 48 h prior to the measurement. Both positive and negative ion spectra were recorded with a TOFSIMS IV instrument from ION-TOF GmbH using a Bi_3^+ gun as the primary source. A 150 × 150 μm^2 area was probed at 45° with respect to the normal of the sample. The employed beam energy and current were 25 keV and 0.3 pA, respectively.

Time-coordinated X-ray photoelectron spectroscopy (XPS) was performed to minimize air exposure of the analyzed samples and to prevent undesired aging effects. The measurements were carried out in the angle-integrated mode using a QUANTES instrument from

https://doi.org/10.1021/acsaelm.1c00219
ACS Appl. Electron. Mater. 2021, 3, 2622−2630

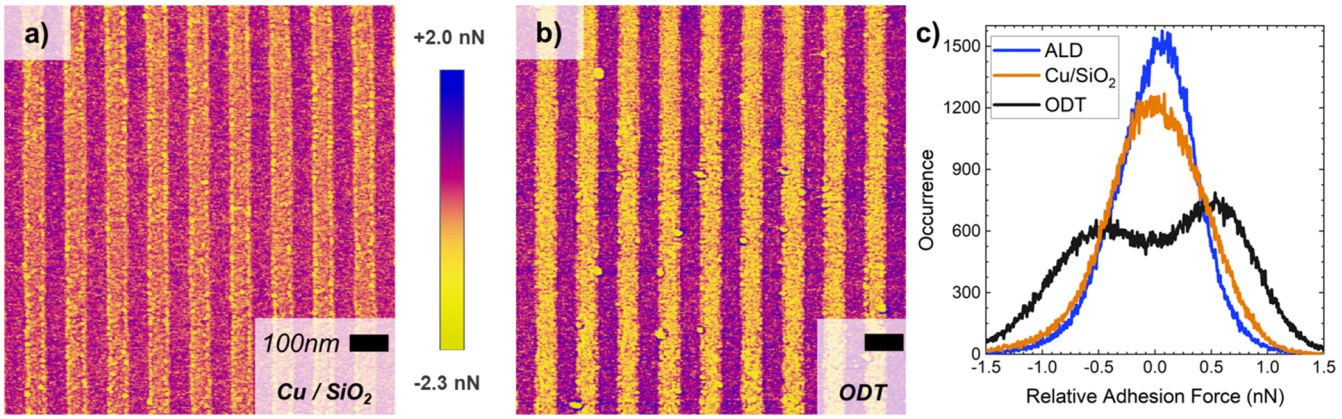

Figure 2. Relative adhesion force maps of a 50 nm-wide Cu/SiO_2 structure after exposure to UV/ozone (a) and upon ODT coating (b). Maps' RAFDs of the 50 nm-wide structure (c): after UV/ozone exposure (orange), upon ODT passivation (black), and after being subjected to a thermal treatment and NH_3 dosing equivalent to 100 Hf_3N_4 ALD cycles at 135 °C (blue). A 5 pN quantization interval is used to compute the RAFDs.

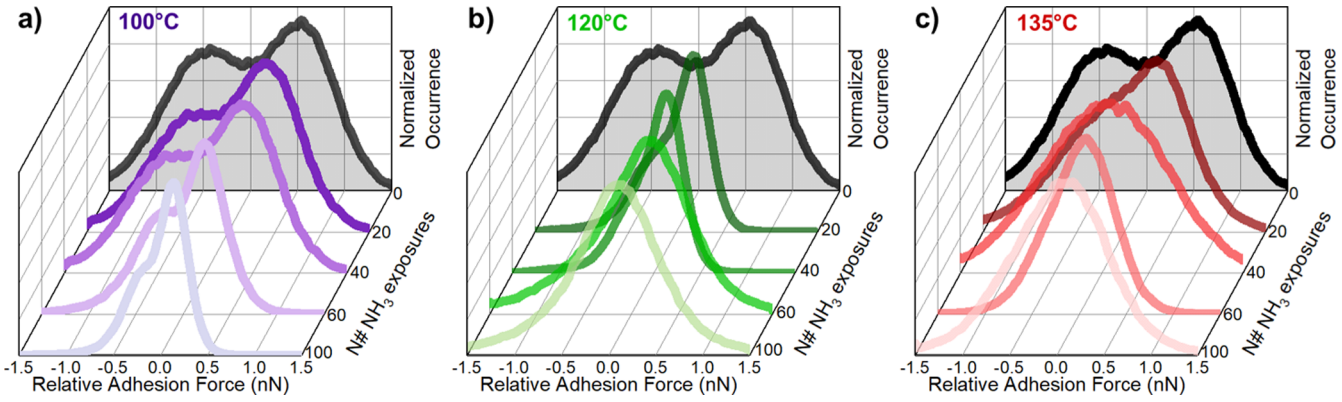

Figure 3. RAFD of the 50 nm-wide Cu/SiO_2 lines passivated with ODT-derived SAM (black). Analogous distributions are plotted from passivated substrates exposed to different temperatures, namely, 100 (a), 120 (b), and 135 °C (c), for a duration and with NH_3 exposures equivalent to 20, 40, 60, and 100 Hf_3N_4 ALD cycles. Occurrences have been normalized to improve plots' readability.

Physical Electronics. XP spectra were collected at exit angles of 45° with respect to the normal of the sample. The measurements were performed using a monochromatized Al Kα X-ray source (1486.6 eV) and a beam size of 20 μm scanned over a ~60 × 300 μm area. The area containing the Cu/SiO_2 pattern was identified by recording X-ray-induced secondary electron images. Charge neutralization was used during this experiment. Standard sensitivity factors were used to convert peak areas to atomic concentrations. Compositional analysis has been shown to have a long-term repeatability close to 1%. Core-level binding energies were calibrated against the C 1s binding energy set at 284.8 eV.[52,53]

ASD Inspection. A Helios NanoLab 460HP FEI SEM tool was used to visualize the top surface of the patterned sample upon Hf_3N_4 ALD, thus assessing the selectivity of the ASD process. The imaging was performed top-down, meaning 0° tilt angle with respect to the sample's normal, with a through-the-lens detector in the secondary electron mode. The 1.28 × 0.85 μm images were collected, with a 10.00 kV applied potential and a probe current varying from 10 to 20 nA. Brightness and contrast corrections were applied using ImageJ software, v 1.52a. This latter was used to perform ALD defectivity estimation as well. In this analysis, the defectivity fraction is defined as the ratio between the total defect area and the Cu lines area, without considering ASD film lateral overgrowth at the Cu line edges as well as defects below a 5 nm diameter (circle-shaped approximation).

RESULTS AND DISCUSSION

Adhesion force maps are initially obtained from 50 nm patterned structures prior to (Figure 2a) and following selective passivation of the Cu lines by ODT-derived SAM (Figure 2b). As the organic layer is selectively deposited on Cu, an adhesion force gradient is observed between the passivated lines and the SiO_2 ones, which are more hydrophilic, leading to darker regions (high adhesion force). Adhesion force maps accurately reflect the surface chemistry, highlighting bright CH_3-terminated hydrophobic regions of the passivated Cu lines and dark lines deriving from strongly oxidized hydrophilic SiO_2 lines after UV/ozone. The adhesion force gradient becomes more evident as RAFDs are plotted (Figure 2c). Prior to Cu selective coating, the 50 nm-wide line structure RAFD is considered unimodal (i.e., homogeneous adhesion force), whereas a bimodal RADF is observed upon SAM selective passivation of the metal lines. It is worth to remark that a small adhesion force contrast is somehow observed between the Cu and SiO_2 lines prior to the ODT-passivation as well (Figure 2a). Nonetheless, the corresponding RAFD (Figure 2c-Cu/SiO_2) does not exhibit two clear components that allows one to confidently claim that the two materials are well-identified by the NM characterization. Conversely, a strong adhesion force contrast (approximately 1.0 nN) is recorded upon ODT selective passivation, which gives rise to a well-separated component in the lower relative adhesion force region of the distribution (Figure 2c-ODT). Since the focus of the NM characterization in this work is to identify the SAM layer from the underneath Cu/SiO_2 substrates, rather than distinguishing metal and dielectric

https://doi.org/10.1021/acsaelm.1c00219
ACS Appl. Electron. Mater. 2021, 3, 2622−2630

lines, the Cu/SiO_2 RAFD prior to passivation is considered purely unimodal.

As the passivated substrate is subjected to NH_3 exposures at 135 °C, for a duration equivalent to 100 Hf_3N_4 ALD cycles, the original unimodal RAFD is reestablished (Figure 2c, blue line), indicating the total ODT depletion under such harsh conditions. During the experiment, the organic film is exposed to the same thermal budget and the same number of NH_3 doses (Figure 1c) of the corresponding Hf_3N_4 ALD process (Figure 1d). In contrast to the ALD process, no Hf-precursor is delivered into the reactor, preventing any material deposition, which would create a topography that interferes with the AFM-enabled NM characterization.

RAFDs are collected from passivated substrates exposed to different temperatures, namely, 100, 120, and 135 °C, for a duration and with an amount of NH_3 exposures equivalent to 20 up to 100 Hf_3N_4 ALD cycles (Figure 3). The adhesion force maps of these patterned samples are reported in Supporting Information S1. As it can be inferred from Figure 3, the initial bimodal character of the passivate substrate's RAFD is progressively lost in favor of a single-peak distribution as the substrates undergo longer and longer thermal treatment with more and more NH_3 doses delivered. It is worth to notice that before turning unimodal, the RAFDs of the passivated substrates subjected to ALD conditions are remarkably right-skewed. The RAFD skewness is a strong indication of the ODT presence being detected. In addition, the distribution's asymmetry appears to be lost as the substrate undergoes longer thermal treatments and it is subjected to more NH_3 doses.

This trend suggests that upon exposure to ALD conditions, more and more ODT molecules become desorbed. Furthermore, such an RAFD bimodal-to-unimodal transition occurs with significant different rates depending on the process temperature: single-peak distributions are observed at earlier stages of the processes at higher temperatures. Specifically, at 100 °C, a bimodal RAFD is seen even after exposing the samples to a process equivalent to 100 Hf_3N_4 ALD cycles (Figure 3a), whereas a unimodal RAFD is observed after a process equivalent to 40 Hf_3N_4 ALD cycles at 135 °C (Figure 3c). The temperature dependence of the RAFD's bimodal-to-unimodal transition suggests that SAM desorption is strongly temperature-dependent as higher process temperatures induce quicker ODT film degradation.

Chemical reactions, such as surface nitridation, between the NH_3 gas and the Cu/SiO_2 substrate could modify the sample's adhesion properties, potentially undermining the NM characterization insights regarding the passivation layer. It is thus important to determine whether the exposure to NH_3 gas has altered the chemical composition of the substrate. SF-SIMS was performed in the past on similar devices to assess the ODT selective chemisorption to Cu versus SiO_2 lines.[54] In this study, SF-SIMS is performed on the passivated substrates prior to and after exposure to ALD conditions as well as on the untreated sample. The aim of the analysis is to identify any potential chemical reactions of NH_3 with the Cu or SiO_2 lines through the presence of Cu−N or Si−N ion clusters. None of these are identified in the spectra, confirming the absence of any reactions at the sensitivity level of the SF-SIMS technique. The only N-containing ions revealed by SF-SIMS analysis with a significant ion count are NH_4^+ and CN^-; these are presented in Supporting Information S4. From these spectra, it can be inferred that the NH_4^+ and CN^- intensities vary randomly between different treatment conditions, validating their identification as contamination components. This eventually confirms that the adhesion force changes detected by the NM characterization are exclusively caused by the progressive thermally activated SAM degradation. In addition, the ODT-related ion count (Supporting Information S4) is observed to progressively drop with the process time and with a strong process temperature dependence, which further supports the temperature-dependent SAM degradation mechanism revealed by NM characterization.

Once ascertained that NH_3-based chemical reactions play no role in altering the substrate's surface properties, quantitative information regarding the passivation layer is obtained by further analyzing the evolution of the RAFD, derived by pulsed force AFM measurements. In eq 1, the ODT fraction (θ_{ODT}) is computed relying on RAFD peak fitting and deconvolution. The following definition is proposed

$$\theta_{ODT} = \frac{A_{ODT}}{A_{tot}} \tag{1}$$

where A_{ODT} and A_{tot} represent the ODT-related peak area of a bimodal RAFD and the total area of the fitted distribution, respectively. All RAFD peak fitting and deconvolution are reported in Supporting Information S3. Based on this definition, θ_{ODT} varies between 0 and 1, depending on whether the ODT layer is completely depleted or fully coating the surface. Clearly, as the RAFD turns unimodal, θ_{ODT} drops to 0. The RAFD-derived ODT fraction on the 50 nm-wide Cu/SiO_2 lines evolution is reported in Figure 4a from samples

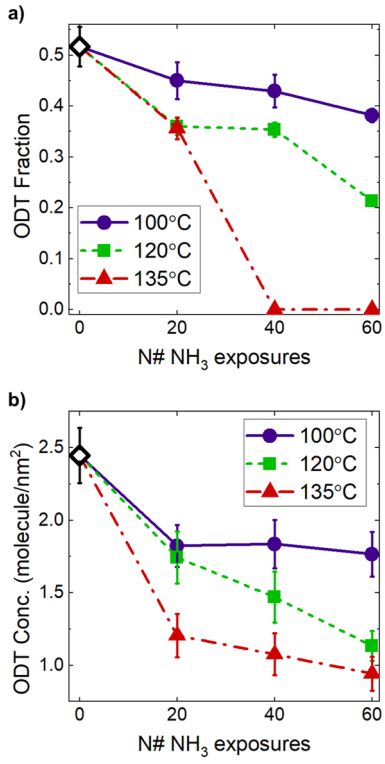

Figure 4. ODT fraction (a) and concentration (b) evolution upon thermal treatments and NH_3 exposures equivalent to 20, 40, and 60 Hf_3N_4 ALD cycles, performed at 100, 120, and 135 °C. The ODT fraction and concentration are derived by NM characterization and XPS measurements, respectively. The hollow diamond-shaped data point is related to a reference SAM-passivated sample subjected to no thermal treatment or NH_3 exposure.

https://doi.org/10.1021/acsaelm.1c00219
ACS Appl. Electron. Mater. 2021, 3, 2622−2630

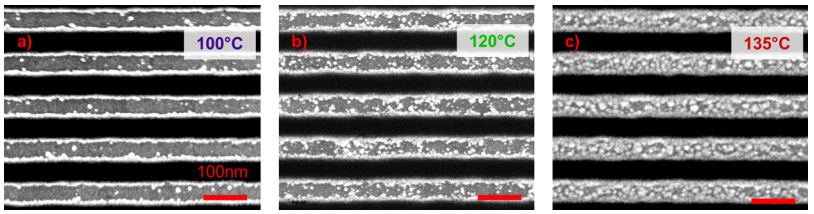

Figure 5. Top-down SEM images of the ODT-passivated 50 nm-wide Cu/SiO_2 lines upon 40 Hf_3N_4 ALD cycles at 100 (a), 120 (b), and 135 °C (c).

exposed to different ALD conditions. Specifically, the SAM coverage is studied by pulsed force AFM measurements as the passivated samples are subjected to an amount of NH_3 dose and an overall process duration, equivalent to 20, 40, and 60 Hf_3N_4 ALD cycles, at 100, 120, and 135 °C.

It is worth noting that, if no ALD-equivalent process is performed on the passivated substrate, the NM characterization predicts an ODT fraction equal to 0.52 ± 0.04 (Figure 4a, black hollow diamond-shaped data point). This is in great agreement with the substrate geometry, which consists of 50 nm-wide metal and dielectric lines and the exclusive chemisorption of ODT on Cu, resulting in half of the surface being covered with SAM precursor molecules (i.e., θ_{ODT} equal to 0.50).

To confirm the coverage trends observed by the NM characterization, XPS is employed to determine the ODT concentration on the 50 nm-wide Cu lines (Γ_{ODT}). This is calculated by monitoring the attenuation of the ODT-related S $2p_{3/2}$ peak in the XP spectra during the ALD-equivalent process according to the following equation[55,56]

$$\Gamma_{ODT} = \frac{A_S}{A_{Cu}}\frac{S_{Cu}}{S_S}\rho_{Cu}\lambda_{Cu}\sin(\varphi)\frac{e^{d/(\lambda_S^{ODT}\sin(\varphi))}}{e^{d/(\lambda_{Cu}^{ODT}\sin(\varphi))}} \quad (2)$$

where A_S/A_{Cu} and S_{Cu}/S_S represent the area ratio of the S $2p_{3/2}$ and Cu $2p_{3/2}$ components in the XP spectra and their atomic sensitivity factors, respectively. In eq 2, ρ_{Cu} is the density of Cu atoms in the cuprous oxide surface (~0.084 mol cm^{-3})[57] and d the ODT thickness (1.5 ± 0.1 nm). The SAM thickness and the presence of cuprous oxide underneath the organic layer were recently discussed in an earlier work from our group.[58] Finally, λ_{Cu} denotes the Cu photoelectron inelastic mean-free path (IMPF, ~0.78 nm) in the substrate,[59] whereas λ_{Cu}^{ODT} and λ_S^{ODT} denote the Cu- and S-related photoelectron's IMFP through the carbonaceous film (~2.12 and ~3.81 nm, respectively),[55] with φ representing the exit angle at which the XP spectra are recorded (45° with respect to the surface's normal). Since Γ_{ODT} is based on the S $2p_{3/2}$ peak associated to the S−Cu bond doublet centered at 162.7 eV, a value in between the binding energy position expected for S bonded to a polymer chain and S bonded to a metal,[52,60] no S-related species but ODT bonded to Cu are considered as the SAM concentration is computed.

Despite XPS is being used to support and corroborate the insight unravelled by the NM characterization, it is worth remarking that these techniques quantify different, although related, properties of the organic film. As pulsed force AFM measurements rely on a macroscopic property such as the film's surface energy, XPS analysis focuses on a microscopic aspect of the organic film: the concentration of the S atom binding energies associated with ODT molecules. Therefore, a quantitative correlation between the SAM precursor concentration and the exhibit surface properties is far from obvious. SAM precursor agglomeration upon thermal treatments, changes in an alkyl chain's configuration due to variation in SAM packing density, or thermally induced ODT degradation are few phenomena that exemplify the complexity behind establishing a direct relationship between the two observables.[33,34] Based on such considerations, in this work, the comparison between pulsed force AFM and XPS measurement results is limited to the observation of overall trends, temperature-dependent phenomena, and detection limits.

Following a thermal treatment with NH_3 exposures that corresponds to 20 Hf_3N_4 ALD cycles, XPS investigation reveals that the ODT has already started to degrade. The thiolate species depletion continues at a rate which is heavily temperature-dependent, as predicted by the NM characterization (Figure 4). Although there is a good agreement between the two characterization techniques, the higher sensitivity of XPS enables ODT detection at low concentration levels, which are inaccessible to pulsed force AFM measurements as RAFDs have turned unimodal already. For instance, if the substrate is subjected to a thermal treatment with NH_3 exposures equivalent to 40 Hf_3N_4 ALD cycles at 135 °C, the presence of 1.08 ± 0.14 molecules per nm^2 is observed by XPS, whereas no ODT contribution is observed in the pulsed force AFM-derived RAFD. Although XPS shows higher sensitivity to ODT detection, it is worth noticing that pulsed force AFM is a less expensive, less complex, and faster analysis method for passivation quality monitoring, which additionally enables direct visualization (Figure 2b) of the SAM layer on patterned structures.

Finally, Hf_3N_4 ALD is performed on the 50 nm-wide Cu/SiO_2 lines. ALD growth per cycle (GPC) as a function of the process temperature is reported in Supporting Information S5. To evaluate the ASD results, top-down SEM images are taken from passivated Cu/SiO_2 lines after 40 Hf_3N_4 ALD cycles at 100, 120, and 135 °C. These are presented and reported in Figure 5. Regardless of the process temperature, ALD defects are detected on the top of Cu. Nevertheless, as the reactor temperature is increased up to 135 °C, the abundance and average size of such unwanted ALD nuclei on the metal lines strongly increase.

Indeed, SEM image analysis reveals that 6.8 ± 0.4, 34.0 ± 1.4, and 59.8 ± 7.5% of the Cu line area is coated with unwanted Hf_3N_4 particles after 40 ALD cycles at 100, 120, and 135 °C, respectively. This examination of Cu/SiO_2 substrates upon Hf_3N_4 ALD agrees with the selectivity loss mechanism predicted by the NM characterization. Indeed, higher process temperatures accelerate the SAM thermally activated degradation, promoting ALD nucleation on the metal lines at an earlier stage of the ASD process. As a result, almost defect-free ASD is observed after 40 ALD cycles only at 100 °C, whereas the metal lines are nearly fully coated in Hf_3N_4 after the same

https://doi.org/10.1021/acsaelm.1c00219
ACS Appl. Electron. Mater. 2021, 3, 2622−2630

amount of ALD cycles performed at 135 °C. Remarkably, after each deposition shown in Figure 5, no dielectric poisoning is observed, which could have prevented Hf_3N_4 from nucleating on SiO_2 regions close to the Cu line edges. This sort of undesired inhibition is observed if the passivation is not tightly confined to the non-growth area (i.e., Cu), for instance, if a multilayer thiol film protrudes over the growth area, as reported by Liu et al.[29] The absence of Hf_3N_4-free patches on SiO_2 indicates that the SAM passivation is limited to the Cu lines only, as highlighted by passivated substrate adhesion force map collected by pulsed force AFM (Figure 2b).

CONCLUSIONS

In conclusion, we have demonstrated an innovative use of pulsed force AFM NM characterization that enables the observation of an organic film on relevant substrates for ASD. It was shown that NM characterization provides complementary information with respect to conventional techniques, such as SEM, TEM, and EDX, for passivation monitoring on heterogeneous surfaces. By exploiting the adhesion force contrast introduced by the selective passivation of the metal lines and its subsequent degradation during the exposure to ALD conditions, the ODT coverage is accurately estimated. These results were supported by XPS analysis of the passivated lines. In addition, SF-SIMS measurements demonstrated that the exposure to NH_3 does not alter the surface composition of the analyzed samples, ensuring that the observed adhesion force modulation is not induced by chemical reactions between the NH_3 gas and the substrate. The insight derived from the NM characterization and SF-SIMS measurements strongly indicates that a thermally activated SAM degradation occurred under the investigated conditions.

Finally, ASD experiments on the 50 nm-wide structures exhibit a strong correlation between the deposition temperature and the abundance of ALD defects nucleating on the Cu lines, highlighting that a process temperature as low as 100 °C leads to the best ASD performance. Hence, monitoring the evolution of the passivation film at relevant nanoscale dimensions during the deposition process is of utmost importance for the ASD application. Indeed, the NM characterization enables understanding the mechanisms responsible for selectivity loss for ASD based on organic inhibitor films.

ASSOCIATED CONTENT

Supporting Information

The Supporting Information is available free of charge at https://pubs.acs.org/doi/10.1021/acsaelm.1c00219.

ODT-passivated 50 nm-wide Cu/SiO_2 line adhesion maps upon NH_3 exposure at 100, 120, and 135 °C for a duration equivalent to 20, 40, 60, and 100 Hf_3N_4 ALD cycles; ODT-passivated 50 nm-wide Cu/SiO_2 line topography maps upon NH_3 exposure at 100, 120, and 135 °C for a duration equivalent to 20, 40, 60, and 100 Hf_3N_4 ALD cycles; RAFD fitting and peak deconvolution of 50 nm-wide Cu/SiO_2 lines prior to and upon organic film passivation and after NH_3 exposures at 100, 120, and 135 °C for a duration equivalent to 20, 40, 60, and 100 Hf_3N_4 ALD cycles; RAFD fitting parameters and results; RAFD fitting parameters and results; NH_4^+, CN^-, and $C_{18}H_{37}S^-$ ion counts by SF-SIMS analysis of ODT-passivated 50 nm-wide Cu/SiO_2 substrates prior to and upon NH_3 exposure at 100 and 135 °C for a duration equivalent to 40 and 100 Hf_3N_4 ALD cycles, UV/ozone exposed Cu/SiO_2 lines are considered as well; Hf_3N_4 thickness as functions of ALD cycles and GPCs for different reactor temperatures (PDF)

AUTHOR INFORMATION

Corresponding Author

Silvia Armini − *Semiconductor Technology and System, Imec, B-3001 Leuven, Belgium*; Email: silvia.armini@imec.be

Authors

Mattia Pasquali − *Department of Chemistry, Faculty of Science, KU Leuven, B-3001 Leuven, Belgium; Semiconductor Technology and System, Imec, B-3001 Leuven, Belgium*; orcid.org/0000-0002-1309-1082

Stefanie Sergeant − *Semiconductor Technology and System, Imec, B-3001 Leuven, Belgium*; orcid.org/0000-0001-9923-0903

Thierry Conard − *Semiconductor Technology and System, Imec, B-3001 Leuven, Belgium*

Valentina Spampinato − *Semiconductor Technology and System, Imec, B-3001 Leuven, Belgium*; orcid.org/0000-0003-3225-6740

Alessandro Viva − *Semiconductor Technology and System, Imec, B-3001 Leuven, Belgium*

Stefan De Gendt − *Department of Chemistry, Faculty of Science, KU Leuven, B-3001 Leuven, Belgium; Semiconductor Technology and System, Imec, B-3001 Leuven, Belgium*

Complete contact information is available at: https://pubs.acs.org/10.1021/acsaelm.1c00219

Author Contributions

The manuscript was written through contributions of all authors. All authors have given approval to the final version of the manuscript.

Notes

The authors declare no competing financial interest.

ACKNOWLEDGMENTS

This project received funding from the Electronic Component Systems for European Leadership Joint Undertaking under grant agreement no 783247. This Joint Undertaking receives support from the European Union's Horizon 2020 research and innovation program and the Netherlands, Belgium, France, Germany, and Israel. The authors acknowledge the contribution of Dr. Alexis Franquet and Dr. Céline Noël regarding the SF-SIMS analysis and Andrea Itziar Pitillas Martinez for designing the graphical abstract's artwork. Finally, the authors acknowledge the helpful insights provided by Dr. Umberto Celano regarding AFM NM characterization.

REFERENCES

(1) Moore, G. E. Cramming More Components onto Integrated Circuits. *Proc. IEEE* **1998**, *86*, 82.

(2) Clark, R.; Tapily, K.; Yu, K.-H.; Hakamata, T.; Consiglio, S.; O'Meara, D.; Wajda, C.; Smith, J.; Leusink, G. Perspective: New Process Technologies Required for Future Devices and Scaling. *APL Mater.* **2018**, *6*, 058203.

(3) Schuegraf, K.; Abraham, M. C.; Brand, A.; Naik, M.; Thakur, R. Semiconductor Logic Technology Innovation to Achieve Sub-10 Nm Manufacturing. *IEEE J. Electron Devices Soc.* **2013**, *1*, 66−75.

(4) Kim, H.; Lee, H.-B.-R.; Maeng, W.-J. Applications of Atomic Layer Deposition to Nanofabrication and Emerging Nanodevices. *Thin Solid Films* **2009**, *517*, 2563−2580.
(5) Parsons, G. N.; Clark, R. D. Area-Selective Deposition: Fundamentals, Applications, and Future Outlook. *Chem. Mater.* **2020**, *32*, 4920−4953.
(6) Mackus, A. J. M.; Merkx, M. J. M.; Kessels, W. M. M. From the Bottom-Up: Toward Area-Selective Atomic Layer Deposition with High Selectivity. *Chem. Mater.* **2019**, *31*, 2−12.
(7) Mackus, A. J. M.; Bol, A. A.; Kessels, W. M. M. The Use of Atomic Layer Deposition in Advanced Nanopatterning. *Nanoscale* **2014**, *6*, 10941−10960.
(8) Lee, H.-B. -R.; Bent, S. F. Nanopatterning by Area-Selective Atomic Layer Deposition. In *Atomic Layer Deposition of Nanostructured Materials*; Pinna, N., Knez, M., Eds.; Wiley-VCH Verlag GmbH & Co. KGaA: Winheim, Germany, 2012; pp 193−225.
(9) Parsons, G. N. Functional Model for Analysis of ALD Nucleation and Quantification of Area-Selective Deposition. *J. Vac. Sci. Technol., A* **2019**, *37*, 020911.
(10) Gladfelter, W. L. Selective Metalization by Chemical Vapor Deposition. *Chem. Mater.* **1993**, *5*, 1372−1388.
(11) Zyulkov, I.; Madhiwala, V.; Voronina, E.; Snelgrove, M.; Bogan, J.; O'Connor, R.; De Gendt, S.; Armini, S. Area-Selective ALD of Ru on Nanometer-Scale Cu Lines through Dimerization of Amino-Functionalized Alkoxy Silane Passivation Films. *ACS Appl. Mater. Interfaces* **2020**, *12*, 4678−4688.
(12) Mameli, A.; Kuang, Y.; Aghaee, M.; Ande, C. K.; Karasulu, B.; Creatore, M.; Mackus, A. J. M.; Kessels, W. M. M.; Roozeboom, F. Area-Selective Atomic Layer Deposition of In_2O_3:H Using a μ-Plasma Printer for Local Area Activation. *Chem. Mater.* **2017**, *29*, 921−925.
(13) Chen, R.; Kim, H.; McIntyre, P. C.; Bent, S. F. Investigation of Self-Assembled Monolayer Resists for Hafnium Dioxide Atomic Layer Deposition. *Chem. Mater.* **2005**, *17*, 536−544.
(14) Hashemi, F. S. M.; Birchansky, B. R.; Bent, S. F. Selective Deposition of Dielectrics: Limits and Advantages of Alkanethiol Blocking Agents on Metal−Dielectric Patterns. *ACS Appl. Mater. Interfaces* **2016**, *8*, 33264−33272.
(15) Hashemi, F. S. M.; Prasittichai, C.; Bent, S. F. Self-Correcting Process for High Quality Patterning by Atomic Layer Deposition. *ACS Nano* **2015**, *9*, 8710−8717.
(16) Zyulkov, I.; Krishtab, M.; De Gendt, S.; Armini, S. Selective Ru ALD as a Catalyst for Sub-Seven-Nanometer Bottom-Up Metal Interconnects. *ACS Appl. Mater. Interfaces* **2017**, *9*, 31031−31041.
(17) Wojtecki, R.; Mettry, M.; Nathel, N. F.; Friz, A.; De Silva, A.; Arellano, N.; Shobha, H. Fifteen Nanometer Resolved Patterns in Selective Area Atomic Layer Deposition—Defectivity Reduction by Monolayer Design. *ACS Appl. Mater. Interfaces* **2018**, *10*, 38630−38637.
(18) Mameli, A.; Merkx, M. J. M.; Karasulu, B.; Roozeboom, F.; Kessels, W. M. M.; Mackus, A. J. M. Area-Selective Atomic Layer Deposition of SiO_2 Using Acetylacetone as a Chemoselective Inhibitor in an ABC-Type Cycle. *ACS Nano* **2017**, *11*, 9303−9311.
(19) Kim, W.-H.; Hashemi, F. S. M.; Mackus, A. J. M.; Singh, J.; Kim, Y.; Bobb-Semple, D.; Fan, Y.; Kaufman-Osborn, T.; Godet, L.; Bent, S. F. A Process for Topographically Selective Deposition on 3D Nanostructures by Ion Implantation. *ACS Nano* **2016**, *10*, 4451−4458.
(20) Färm, E.; Kemell, M.; Ritala, M.; Leskelä, M. Selective-Area Atomic Layer Deposition with Microcontact Printed Self-Assembled Octadecyltrichlorosilane Monolayers as Mask Layers. *Thin Solid Films* **2008**, *517*, 972−975.
(21) Bobb-Semple, D.; Nardi, K. L.; Draeger, N.; Hausmann, D. M.; Bent, S. F. Area-Selective Atomic Layer Deposition Assisted by Self-Assembled Monolayers: A Comparison of Cu, Co, W, and Ru. *Chem. Mater.* **2019**, *31*, 1635−1645.
(22) Lecordier, L.; Herregods, S.; Armini, S. Vapor-Deposited Octadecanethiol Masking Layer on Copper to Enable Area Selective Hf_3N_4 Atomic Layer Deposition on Dielectrics Studied by in Situ Spectroscopic Ellipsometry. *J. Vac. Sci. Technol., A* **2018**, *36*, 031605.
(23) Khan, R.; Shong, B.; Ko, B. G.; Lee, J. K.; Lee, H.; Park, J. Y.; Oh, I.-K.; Raya, S. S.; Hong, H. M.; Chung, K.-B.; Luber, E. J.; Kim, Y.-S.; Lee, C.-H.; Kim, W.-H.; Lee, H.-B.-R. Area-Selective Atomic Layer Deposition Using Si Precursors as Inhibitors. *Chem. Mater.* **2018**, *30*, 7603−7610.
(24) Zyulkov, I.; Voronina, E.; Krishtab, M.; Voloshin, D.; Chan, B. T.; Mankelevich, Y.; Rakhimova, T.; Armini, S.; De Gendt, S. Area-Selective Ru ALD by Amorphous Carbon Modification Using H Plasma: From Atomistic Modeling to Full Wafer Process Integration. *Mater. Adv.* **2020**, *1*, 3049.
(25) Vallat, R.; Gassilloud, R.; Salicio, O.; El Hajjam, K.; Molas, G.; Pelissier, B.; Vallée, C. Area Selective Deposition of TiO_2 by Intercalation of Plasma Etching Cycles in PEALD Process: A Bottom up Approach for the Simplification of 3D Integration Scheme. *J. Vac. Sci. Technol., A* **2019**, *37*, 20918.
(26) Soethoudt, J.; Grillo, F.; Marques, E. A.; van Ommen, J. R.; Tomczak, Y.; Nyns, L.; Van Elshocht, S.; Delabie, A. Diffusion-Mediated Growth and Size-Dependent Nanoparticle Reactivity during Ruthenium Atomic Layer Deposition on Dielectric Substrates. *Adv. Mater. Interfaces* **2018**, *5*, 1800870.
(27) Grillo, F.; Moulijn, J. A.; Kreutzer, M. T.; van Ommen, J. R. Nanoparticle Sintering in Atomic Layer Deposition of Supported Catalysts: Kinetic Modeling of the Size Distribution. *Catal. Today* **2018**, *316*, 51−61.
(28) Pasquali, M.; De Gendt, S.; Armini, S. Area-Selective Deposition by a Combination of Organic Film Passivation and Atomic Layer Deposition. *ECS Trans.* **2019**, *92*, 25−32.
(29) Liu, T.-L.; Nardi, K. L.; Draeger, N.; Hausmann, D. M.; Bent, S. F. Effect of Multilayer versus Monolayer Dodecanethiol on Selectivity and Pattern Integrity in Area-Selective Atomic Layer Deposition. *ACS Appl. Mater. Interfaces* **2020**, *12*, 42226−42235.
(30) Minjauw, M. M.; Rijckaert, H.; Driessche, I. V.; Detavernier, C.; Dendooven, J. Nucleation Enhancement and Area-Selective Atomic Layer Deposition of Ruthenium Using RuO_4 and H_2 Gas. *Chem. Mater.* **2019**, *31*, 1491−1499.
(31) Vos, M. F. J.; Chopra, S. N.; Verheijen, M. A.; Ekerdt, J. G.; Agarwal, S.; Kessels, W. M. M.; Mackus, A. J. M. Area-Selective Deposition of Ruthenium by Combining Atomic Layer Deposition and Selective Etching. *Chem. Mater.* **2019**, *31*, 3878−3882.
(32) Guo, L.; Qin, X.; Zaera, F. Chemical Treatment of Low-k Dielectric Surfaces for Patterning of Thin Solid Films in Microelectronic Applications. *ACS Appl. Mater. Interfaces* **2016**, *8*, 6293−6300.
(33) Ulman, A. Formation and Structure of Self-Assembled Monolayers. *Chem. Rev.* **1996**, *96*, 1533−1554.
(34) Love, J. C.; Estroff, L. A.; Kriebel, J. K.; Nuzzo, R. G.; Whitesides, G. M. Self-Assembled Monolayers of Thiolates on Metals as a Form of Nanotechnology. *Chem. Rev.* **2005**, *105*, 1103−1170.
(35) Färm, E.; Vehkamäki, M.; Ritala, M.; Leskelä, M. Passivation of Copper Surfaces for Selective-Area ALD Using a Thiol Self-Assembled Monolayer. *Semicond. Sci. Technol.* **2012**, *27*, 074004.
(36) Sampson, M. D.; Emery, J. D.; Pellin, M. J.; Martinson, A. B. F. Inhibiting Metal Oxide Atomic Layer Deposition: Beyond Zinc Oxide. *ACS Appl. Mater. Interfaces* **2017**, *9*, 33429−33436.
(37) Schnieders, H.; Ozcan, O.; Grundmeier, G. Self-Localization of Mixed Organophosphonic Acid and Organothiol Monolayers on Patterned Al-Cu Substrates. *Appl. Surf. Sci.* **2013**, *287*, 397−403.
(38) Bergsman, D. S.; Liu, T.-L.; Closser, R. G.; Nardi, K. L.; Draeger, N.; Hausmann, D. M.; Bent, S. F. Formation and Ripening of Self-Assembled Multilayers from the Vapor-Phase Deposition of Dodecanethiol on Copper Oxide. *Chem. Mater.* **2018**, *30*, 5694−5703.
(39) Krotil, H.-U.; Stifter, T.; Waschipky, H.; Weishaupt, K.; Hild, S.; Marti, O. Pulsed Force Mode: A New Method for the Investigation of Surface Properties. *Surf. Interface Anal.* **1999**, *27*, 336−340.
(40) Rosa-Zeiser, A.; Weilandt, E.; Hild, S.; Marti, O. Simultaneous Measurement of Elastic, Electrostatic and Adhesive Properties by Scanning Force Microscopy: Pulsed-Force Mode Operation. *Meas. Sci. Technol.* **1997**, *8*, 1333−1338.

https://doi.org/10.1021/acsaelm.1c00219
ACS Appl. Electron. Mater. 2021, 3, 2622−2630

(41) Cappella, B.; Dietler, G. Force-Distance Curves by Atomic Force Microscopy. *Surf. Sci. Rep.* **1999**, *34*, 1−104.
(42) Yang, C.-W.; Chen, C.-H.; Ding, R.-F.; Liao, H.-S.; Hwang, I.-S. Multiparametric Characterization of Heterogeneous Soft Materials Using Contact Point Detection-Based Atomic Force Microscopy. *Appl. Surf. Sci.* **2020**, *522*, 146423.
(43) Krieg, M.; Fläschner, G.; Alsteens, D.; Gaub, B. M.; Roos, W. H.; Wuite, G. J. L.; Gaub, H. E.; Gerber, C.; Dufrêne, Y. F.; Müller, D. J. Atomic Force Microscopy-Based Mechanobiology. *Nat. Rev. Phys.* **2019**, *1*, 41−57.
(44) Chen, Q.; Liu, J.; Thundat, T.; Gray, M. R.; Liu, Q. Spatially Resolved Organic Coating on Clay Minerals in Bitumen Froth Revealed by Atomic Force Microscopy Adhesion Mapping. *Fuel* **2017**, *191*, 283−289.
(45) Aoki, T.; Ito, K.; Yokoyama, H. Adhesion Force Analysis of Dynamic Polymer Brushes. *Langmuir* **2020**, *36*, 6210−6215.
(46) Sababi, M.; Kettle, J.; Rautkoski, H.; Claesson, P. M.; Thormann, E. Structural and Nanomechanical Properties of Paperboard Coatings Studied by Peak Force Tapping Atomic Force Microscopy. *ACS Appl. Mater. Interfaces* **2012**, *4*, 5534−5541.
(47) Fakhrullina, G.; Akhatova, F.; Kibardina, M.; Fokin, D.; Fakhrullin, R. Nanoscale Imaging and Characterization of Caenorhabditis Elegans Epicuticle Using Atomic Force Microscopy. *Nanomed. Nanotechnol. Biol. Med.* **2017**, *13*, 483−491.
(48) Heu, C.; Berquand, A.; Elie-Caille, C.; Nicod, L. Glyphosate-Induced Stiffening of HaCaT Keratinocytes, a Peak Force Tapping Study on Living Cells. *J. Struct. Biol.* **2012**, *178*, 1−7.
(49) Rico, F.; Su, C.; Scheuring, S. Mechanical Mapping of Single Membrane Proteins at Submolecular Resolution. *Nano Lett.* **2011**, *11*, 3983−3986.
(50) Su, C.; Shi, J.; Hu, Y.; Hu, S.; Ma, J. Method and Apparatus of Using Peak Force Tapping Mode to Measure Physical Properties of a Sample. U.S. Patent 9,291,640 B2, 2008.
(51) O'Haver, T. Pragmatic Introduction to Signal Processing. https://terpconnect.umd.edu/?toh/spectrum/TOC.html (accessed Nov 16, 2020).
(52) NIST. X-ray Photoelectron Spectroscopy (XPS) Dataset. https://srdata.nist.gov/xps (accessed Feb 1, 2021).
(53) Shchukarev, A.; Korolkov, D. XPS Study of Group IA Carbonates. *Cent. Eur. J. Chem.* **2004**, *2*, 347−362.
(54) Spampinato, V.; Armini, S.; Franquet, A.; Conard, T.; van der Heide, P.; Vandervorst, W. Self-Focusing SIMS: A Metrology Solution to Area Selective Deposition. *Appl. Surf. Sci.* **2019**, *476*, 594−599.
(55) Kim, H.; Colavita, P. E.; Paoprasert, P.; Gopalan, P.; Kuech, T. F.; Hamers, R. J. Grafting of Molecular Layers to Oxidized Gallium Nitride Surfaces via Phosphonic Acid Linkages. *Surf. Sci.* **2008**, *602*, 2382−2388.
(56) Rechmann, J.; Krzywiecki, M.; Erbe, A. Carbon−Sulfur Bond Cleavage During Adsorption of Octadecane Thiol to Copper in Ethanol. *Langmuir* **2019**, *35*, 6888−6897.
(57) Deroubaix, G.; Marcus, P. X-ray Photoelectron Spectroscopy Analysis of Copper and Zinc Oxides and Sulphides. *Surf. Interface Anal.* **1992**, *18*, 39−46.
(58) Pasquali, M.; De Gendt, S.; Armini, S. Understanding the Impact of Cu Surface Pre-Treatment on Octadecanethiol-Derived Self-Assembled Monolayer as a Mask for Area-Selective Deposition. *Appl. Surf. Sci.* **2021**, *540*, 148307.
(59) Powell, C. J.; Jablonski, A. Evaluation of Calculated and Measured Electron Inelastic Mean Free Paths near Solid Surfaces. *J. Phys. Chem. Ref. Data* **1999**, *28*, 19−62.
(60) Laibinis, P. E.; Whitesides, G. M. ω-Terminated Alkanethiolate Monolayers on Surfaces of Copper, Silver, and Gold Have Similar Wettabilities. *J. Am. Chem. Soc.* **1992**, *114*, 1990−1995.

https://doi.org/10.1021/acsaelm.1c00219
ACS Appl. Electron. Mater. 2021, 3, 2622−2630